Composites: Part A 51 (2013) 11–21

Contents lists available at SciVerse ScienceDirect

Composites: Part A

journal homepage: www.elsevier.com/locate/compositesa

A model for fiber length attrition in injection-molded long-fiber composites

Jay H. Phelps [a], Ahmed I. Abd El-Rahman [a], Vlastimil Kunc [b], Charles L. Tucker III [a,*]

[a] Department of Mechanical Science and Engineering, University of Illinois at Urbana-Champaign, Urbana, IL 61801, USA
[b] Oak Ridge National Laboratory, Oak Ridge, TN, USA

ARTICLE INFO

Article history:
Received 20 January 2013
Received in revised form 1 April 2013
Accepted 2 April 2013
Available online 12 April 2013

Keywords:
A. Discontinuous reinforcement
B. Microstructures
C. Computational modeling
E. Injection moulding

ABSTRACT

Long-fiber thermoplastic (LFT) composites consist of an engineering thermoplastic matrix with glass or carbon reinforcing fibers that are initially 10–13 mm long. When an LFT is injection molded, flow during mold filling degrades the fiber length. Here we present a detailed quantitative model for fiber length attrition in a flowing fiber suspension. The model tracks a discrete fiber length distribution at each spatial node. A conservation equation for total fiber length is combined with a breakage rate that is based on buckling of fibers due to hydrodynamic forces. The model is combined with a mold filling simulation to predict spatial and temporal variations in fiber length distribution in a mold cavity during filling. The predictions compare well to experiments on a glass–fiber/PP LFT molding. Fiber length distributions predicted by the model are easily incorporated into micromechanics models to predict the stress–strain behavior of molded LFT materials.

© 2013 Elsevier Ltd. All rights reserved.

1. Introduction

Long-fiber thermoplastic composites (or LFTs) bridge the gap between short- and continuous-fiber thermoplastic composites, offering better mechanical properties than short-fiber materials but retaining the ability to be injection molded. LFTs, under the trade name of Verton, were developed in the mid-1980s by Imperial Chemical Industries of the United Kingdom, and initially consisted of a polyamide 6,6 matrix reinforced with glass fibers [1,2]. To date, glass remains the most common reinforcing material, but carbon is seen as well [3–5]. Other matrix materials have included polypropylene [6–8,4,9–11], polyethylene terephthalate [7,12], polybutylene terephthalate [12], polyphthalamide [13,14], polycarbonate [14], polyphenylene sulfide [14], and blends of polycarbonate or polyamide 6,6 with polytetrafluoroethylene [14]. Mechanical property improvements over short-fiber plastics have been significant, and the ability to injection mold these materials has been preserved.

LFT pellets are usually prepared by a pultrusion process, in which continuous fibers with a polymer matrix surrounding them are pulled through a circular die. As the resulting fiber-filled strand solidifies, it may be sliced into individual pellets. These pellets are typical 2–3 mm in diameter and 10–13 mm long, with 10–13 mm long fibers aligned along their length. This is a dramatic contrast to the 0.2–0.4 mm long, randomly oriented fibers in short-fiber pellets [2].

Processing affects the microstructure of LFTs, just as it does with other composite materials. For LFTs the main microstructural variables are fiber orientation and fiber length. Fiber orientation for LFTs can be modeled using conventional moment tensor equations [15–17], and at least one special fiber orientation model had been developed to better capture some of the quantitative details of LFT fiber orientation [18].

Regarding fiber length, a number of experimental studies have examined changes in fiber length in LFT materials. The fibers in an LFT initially have the length of the pellet, 10–13 mm, but few fibers with this length survive in an injection-molded part. While fibers may break during any stage of the injection molding process, Bailey and Kraft [6] found that significant attrition occurs before the polymer melt enters the mold. Thus, most experimental studies examine fiber breakage as a function of process parameters such as screw back pressure, injection speed, gate size, and nozzle design.

Bailey and Kraft [6] and Vu-Khanh et al. [12] found that 10 mm long glass fibers in a polyamide matrix were reduced to lengths of approximately 1 mm by the end of the molding process, with mean fiber lengths no greater than 1.6 mm at the screw exit (i.e., before entering the mold). However, moldings made with a polypropylene matrix had mean fiber lengths two to three times greater than with polyamide matrices. In an edge-gated disk molding of unspecified thickness, Bailey and Kraft [6] found mean fiber lengths in the inner core to be three times those of the skin layer, a phenomenon attributed to the high shear rates in the skin during mold filling.

* Corresponding author. Tel.: +1 217 244 3822.
E-mail address: ctucker@illinois.edu (C.L. Tucker III).

1359-835X/$ - see front matter © 2013 Elsevier Ltd. All rights reserved.
http://dx.doi.org/10.1016/j.compositesa.2013.04.002

Mean fiber lengths on the order of 1 mm were also observed by Vu-Khanh et al. [12] for 6 mm thick rectangular plate moldings (124 mm × 67 mm) with polybutylene terephthalate and polyethylene terephthalate matrices. O'Regan and Akay [19] and LaFranche et al. [20] also give typical fiber lengths for both plate moldings and more complex production parts. O'Regan and Akay also found skin/core differences in fiber length, and the fiber length decreased along the flow path, in some cases by as much as 30%.

Significant fiber length degradation also occurs in compounding equipment, as shown by a number of experimental studies. This literature is nicely reviewed by Inceoglu et al. [21]. One key observation is that changes in fiber length are primarily dependent on total strain, at least within a modest range of stress levels [22,21]. Also, if the stress level is substantially reduced, then the average fiber length will degrade more slowly [22].

In contrast to the large number of experiments, very little has been done to model changes in fiber length during processing. Shon et al. [23] proposed a model for compounding devices in which an average fiber length L decreased toward an equilibrium value L_∞ according to

$$\frac{dL}{dt} = -k_f(L - L_\infty) \tag{1}$$

Shon and co-workers did not specify how the average length L is defined, nor how one might predict the model parameters L_∞ and k_f. They used the kinetic constant k_f as a fitting parameter, and reported k_f values for different compounding devices as a way of describing the performance of those devices.

Inceoglu et al. [21] provided experimental data showing how the weight-average fiber length L_w progresses with time or strain, verifying the exponential decrease in fiber length predicted by Shon et al.'s model. They also suggested that specific mechanical energy (SME) is a useful parameter for correlating the rates of fiber length degradation in different devices. They proposed an extension of Shon et al.'s model,

$$\frac{dL_w}{dt} = -K''\mathrm{SME}(L_w - L_{w\infty}) \tag{2}$$

Using SME allowed Inceoglu et al. to collapse data from both lab-scale and production-scale twin-screw extruders onto a single curve, but a ten-fold change in the rate constant K'' was required to represent the data for a batch mixer, which operates at much lower stress levels.

A much more sophisticated model for fiber length attrition was recently reported by Durin et al. [24], while this article was in initial review. That model and the one we present here are closely related, and should produce similar results. We will discuss the model of Durin et al. in more detail in Section 2.6, after presenting our model.

In this study, we develop a quantitative, mechanistic model to predict changes in fiber length distribution during the molding of LFT composites, and compare the predictions of that model to molding experiments. Having a model that accounts for the roles of stress and total strain is particularly important for injection molding, where the stress and shear rate levels vary dramatically across the cavity thickness. Also, having a model that predicts the entire fiber length distribution allows more accurate prediction of mechanical properties, especially strength and fracture toughness.

We apply our model to study changes in fiber length caused by flow in the runner system and mold cavity, and defer the modeling of the injection unit. In most manufacturing situations the screw selection and plasticizing conditions are relatively stable across a variety of parts, while the mold cavity geometry will vary greatly. Thus, being able to model the effect of part geometry on fiber length is a good first goal in developing predictive models for fiber length. Focusing on the cavity flow also allows us to take a "continuum" approach, which is appropriate for a first model. We recognize that some special, non-local treatment of the melting zone of the screw, and of geometric features like gates and sharp bends in runners, may have to be added to create a complete model for fiber length.

2. Theory

The main steps in developing the theory are to select appropriate variables to describe the microstructure; write the balance equation for these variables; and develop constitutive equations as needed to describe the process dynamics. The resulting theory can then be implemented in a mold filling simulation.

2.1. Microstructural variables

The microstructure at any position within the flow is described by a discrete approximation to the fiber length distribution. Choose a finite increment of fiber length $\Delta\ell$, and let $\ell_i = i\Delta\ell$ be a set of discrete length values. i ranges from 1 to n, where n is large enough that ℓ_n is greater than or equal to the initial fiber length in the pellets. One should also choose $\Delta\ell = \ell_1$ to be smaller than the shortest fiber that will break during the flow. This is not a strict requirement, but without this the model may not conserve total fiber length.

Now let N_i represent the expected value of the number of fibers of length ℓ_i in a sample taken from a small region. Alternately, the N_i values can be regarded as proportional to the expected number of fibers of length ℓ_i per unit volume. The set of N_i values, $i = 1$ to n, represents the local fiber length distribution. While it is common to normalize the fiber length distribution function N_i, we do not assume any particular normalization of this function in what follows.

An alternate way to describe fiber length distributions is to use a weight-based distribution function, w_i. This is related to the number-based distribution function by

$$w_i = \kappa N_i \ell_i \tag{3}$$

where κ is any convenient normalization constant. Often κ is chosen to make $\sum w_i = 1$.

Length distribution data is often summarized by giving an average length value. Here one must be careful to distinguish how the average is computed. The number-average fiber length L_n is

$$L_n = \frac{\sum N_i \ell_i}{\sum N_i}, \tag{4}$$

while the weight-average (or length-average) fiber length L_w is

$$L_w = \frac{\sum N_i \ell_i^2}{\sum N_i \ell_i}. \tag{5}$$

It is always true that $L_w \geqslant L_n$, with the equality applying when all fibers have the same length. In analogy with the polydispersity index for polymer molecular weights, one could characterize the breadth of the fiber length distribution by the ratio L_w/L_n, though this idea has not been widely used.

In studying models for the fiber length distribution it is also helpful to define a total fiber length:

$$L_t = \sum N_i \ell_i \tag{6}$$

The value of L_t is arbitrary, depending on the normalization of N_i, but any model for the fiber length distribution should maintain a constant value of L_t.

Fig. 1 shows an experimental fiber length distribution for one of the samples in our study. The distribution of lengths is quite broad, with a few fibers of 12 mm or longer remaining in the sample, even

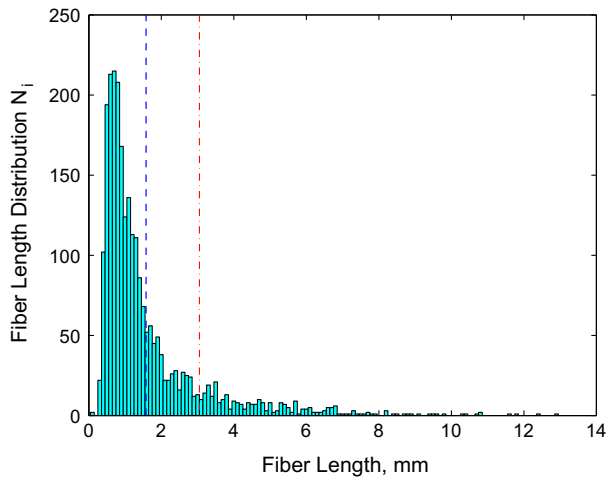

Fig. 1. Experimental fiber length distribution at position A for sample AF3D. Vertical lines indicate the number-average fiber length $L_n = 1.58$ mm and the weight-average fiber length $L_w = 3.05$ mm. (For interpretation of the references to color in this figure legend, the reader is referred to the web version of this article.)

though the majority of the fibers are less than 2 mm long. Very similar experimental distributions have been shown in the literature [22,21]. The number-average and weight-average fiber lengths are also shown in this figure.

Micromechanics theories can predict the properties of LFTs and other composites as a function of the fiber length, volume fraction, and orientation, as well as the fiber and matrix properties. Such theories can either use a single average value of length, or they can use the complete length distribution N_i [25]. Since the average length values can easily be calculated from the N_i values, either type of micromechanics calculation can use the results from our fiber length model.

2.2. Conservation of total length

The basic equation that governs the dynamics of the fiber length distribution expresses how N_i changes as fibers break. To write this equation we must define the rate at which *parent* fibers break, and the corresponding rate at which new, shorter *children* fibers are formed. Consider a time interval Δt, and define the *breakage rate* P_i such that $P_i\Delta t$ is the probability that a fiber of length ℓ_i will break over the time interval Δt. Similarly, define the *child generation rate* R_{ji} such that the probability of generating a child fiber of length ℓ_j over the interval Δt by breaking a parent fiber of length ℓ_i is $R_{ji}\Delta t$.

We assume that all breakage events involve a single fiber breaking into two smaller fibers. Consider a fiber of length ℓ_i that breaks into two children, with lengths ℓ_j and ℓ_k. Since total fiber length is conserved, we must have $\ell_j + \ell_k = \ell_i$, or $j + k = i$. The probability of these two child fibers being created must be the same, so the child generation rate must satisfy

$$R_{ki} = R_{(i-k)i} \tag{7}$$

For example, $R_{6,10} = R_{4,10}$. Also, the sum of the rates of creating all possible child fibers from parents of a given length, say ℓ_i, is determined by the probability of breaking that parent fiber. Accounting for the fact that each break of a parent creates two children, this requires that

$$\sum_j R_{ji} = 2P_i \tag{8}$$

Because shorter fibers never re-combine to produce longer fibers, we also know that $R_{ji} = 0$ for all $j \geqslant i$.

Now consider the fibers of length ℓ_i in a small volume of material. Within some normalization factor there are N_i such fibers. Over a time Δt we would expect $P_iN_i\Delta t$ of these fibers to break, thus decreasing the value of N_i. N_i could also increase, when longer fibers break to produce children of length ℓ_i. The contribution of parent fibers with length ℓ_k to children of length ℓ_i would be $R_{ik}N_k\Delta t$. The total rate of child generation is formed by summing this over all possible parent lengths ℓ_k.

Combining the loss due to breakage with the growth due to generation of children gives a basic conservation equation for N_i:

$$\frac{dN_i}{dt} = -P_iN_i + \sum_k R_{ik}N_k \tag{9}$$

This is the basic conservation equation for fiber length.

Using Eq. (9) one can write an equation for the rate of change of total length, L_t (see Eq. (6)). One can then show that if Eqs. (7) and (8) hold, $dL_t/dt = 0$, and total fiber length is conserved [26].

2.3. Fiber breakage rate

The next step is to develop a constitutive equation that gives the breakage rate P_i as a function of flow conditions and fiber properties. Our initial model is based on hydrodynamic loading of a single fiber. In an LFT, as in most practical fiber composites, each fiber will also have contact or near-contact with a number of neighboring fibers, and this may affect the breakage rate. Some models exist for the frequency and number of short-range contacts [27], and for sliding forces at fiber–fiber contacts [28]. However, at present there is not a good model for normal forces due to fiber–fiber contacts. Also, the effect of the contact forces on total fiber loading is unclear. While hydrodynamic loading can place a fiber in compression (causing buckling, the presumed mode of failure) or tension, it is not known if the individual contact forces increase or decrease the effects of the hydrodynamic loading. For instance, normal forces from contacts may promote bending in fibers, but these forces also drive the formation of fiber networks, which may support individual fibers and prevent breakage. What can be safely assumed, however, is that the presence of even slight contact forces may trigger buckling from the compressive forces of a hydrodynamically loaded fiber. With this assumption, we choose as a first step to focus on the hydrodynamic forces acting on a fiber. This approach is consistent with the findings of von Turkovich and Erwin [29], who suggested that dilute-suspension models of fiber buckling can account for observed data on fiber breakage.

Prior research into the effect of hydrodynamic loadings on fibers in suspension has largely been focused on calculating bulk stress and suspension viscosity. In this context, Dinh and Armstrong [30] used continuum mechanics arguments to develop a model for the effects of hydrodynamic loading of fibers on bulk viscosity. Shaqfeh and Fredrickson [31] also developed a stress model using particle scattering theory, and this model has been preferred in more recent studies [27]. However, we are most concerned with a model for intra-fiber forces, and the classical work of Dinh and Armstrong is convenient for our needs.

Consider a fiber of length ℓ_i whose long axis is oriented parallel to the unit vector **p**. Following Dinh and Armstrong [30] and other fiber suspension models, the fiber will be loaded in tension or compression, in proportion to the stretching or contraction rate parallel to the fiber axis. This rate is given by **D**: **pp**, where **D** is the rate-of-deformation tensor, $D_{mn} = \frac{1}{2}(\partial v_m/\partial x_n + \partial v_n/\partial x_m)$.

In regions of simple shear flow, like the shell region of injection-molded composites, individual fibers in suspension reach a near steady-state orientation where the axis of the fiber is canted slightly in relation to the flow direction, and where **D**:**pp** > 0. In this orientation, the fiber is in tension. Then, through a process known

as a Jeffery orbit, the individual fibers periodically flip, and may rotate through a region in orientation space where $\mathbf{D}:\mathbf{pp} < 0$, placing the fiber in compression. Thus, collections of suspended fibers undergoing simple shear deformation are primarily loaded in tension, but individual fibers will periodically be placed in compression. This is the mechanism by which fibers buckle in a simple shear flow [29,32–35]. For a brittle fiber, buckling will cause the fiber to break.

Using the slender-body analysis of Dinh and Armstrong [30], one can show that the magnitude of the compressive force at the center of a fiber oriented in direction $\mathbf{p}$ is

$$F_i(\mathbf{p}) = \frac{\zeta \eta_m \ell_i^2}{8}(-\mathbf{D}:\ \mathbf{pp}) \tag{10}$$

Details are given in Appendix A. Here ζ is a dimensionless drag coefficient and η_m is the viscosity of the polymer matrix. Note that $F_i(\mathbf{p})$ is positive when $\mathbf{D}:\ \mathbf{pp} < 0$ and the fiber is in compression.

From classical Euler buckling theory, the critical force to cause an end-loaded fiber to buckle is

$$F_{\text{crit}} = \frac{\pi^3 E_f d_f^4}{64 \ell_i^2} \tag{11}$$

Here E_f is the elastic modulus of the fiber and d_f is the fiber diameter.

We expect that a fiber will buckle if $F_i > F_{\text{crit}}$. Combining Eqs. (10) and (11), we expect buckling if

$$\frac{F_i(\mathbf{p})}{F_{\text{crit}}} = B_i(-2\widehat{\mathbf{D}}:\ \mathbf{pp}) \geqslant 1 \tag{12}$$

Here B_i is a dimensionless variable for fiber buckling, dependent on the fiber length ℓ_i and defined as

$$B_i \equiv \frac{4\zeta \eta_m \dot{\gamma} \ell_i^4}{\pi^3 E_f d_f^4} \tag{13}$$

Also, $\dot{\gamma}$ is the scalar magnitude of $\mathbf{D}$, and $\widehat{\mathbf{D}}$ is a dimensionless rate-of-deformation tensor,

$$\widehat{\mathbf{D}} \equiv \mathbf{D}/\dot{\gamma} \tag{14}$$

We can see in Eq. (12) that B_i combines many of the physical parameters of the problem into a single dimensionless variable. Note that the shear stress $(\eta_m \dot{\gamma})$ appears in the numerator, and that the fiber aspect ratio ℓ_i/d_f is raised to the fourth power. The elastic modulus E_f is the only fiber property that appears, because buckling is an elastic instability governed by the stiffness of the fiber, rather than by its strength.

The $(-2\widehat{\mathbf{D}}:\ \mathbf{pp})$ term in Eq. (12) depends on of the type of deformation (shear flow, elongational flow, etc.) and the orientation of the fiber relative to that deformation. The orientation dependence of this term for simple shear flow is shown in Fig. 2. Fibers experience maximum compression when $\mathbf{p}$ lies in the flow/gradient plane and is oriented at $-45°$ or $135°$ to the flow direction (the red zones in the figure). The value of $(-2\widehat{\mathbf{D}}:\ \mathbf{pp})$ at this orientation is unity. Thus, for $B_i < 1$, there is no direction $\mathbf{p}$ in which the fiber satisfies the buckling criterion, and the fiber cannot be broken. For any given set of parameters, the fiber length below which $B_i < 1$ is an unbreakable length.

The more interesting case occurs when $B_i > 1$. Now there is a set of orientations at which a fiber can be broken. The size of this region in Fig. 2 will increase as B_i increases, though the region never occupies more than half the area of the sphere.

With this in mind, there are several ways to interpret B_i physically. If we imagine varying the shear rate while holding all other parameters constant, then we can define the critical shear rate that is just able to break a fiber of length ℓ_i as

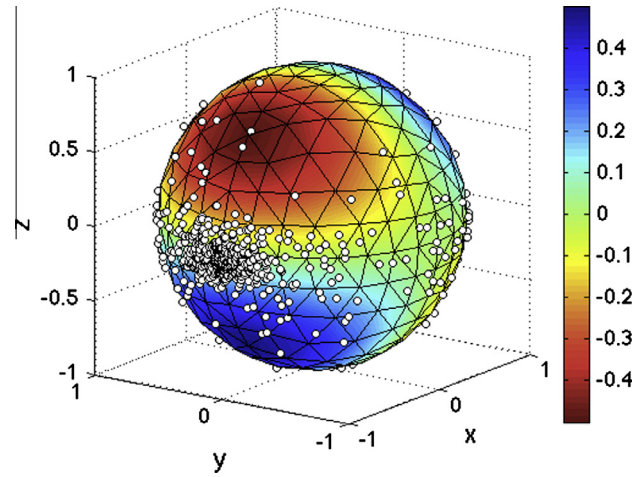

Fig. 2. Sphere of all possible fiber directions $\mathbf{p}$, colored by the value of $(\mathbf{D}:\ \mathbf{pp})$ for the simple shear flow $v_x = \dot{\gamma}z$. Negative values (red to yellow colors) indicate orientations where the fiber is in compression. Points on the sphere are a sample of fiber orientations at steady state for this flow, calculated using the Folgar–Tucker model.

$$\dot{\gamma}_{\text{crit},i} = \frac{\pi^3 E_f d_f^4}{4\zeta \eta_m \ell_i^4} \tag{15}$$

and we see that B_i is the ratio between the actual shear rate and this critical shear rate,

$$B_i = \dot{\gamma}/\dot{\gamma}_{\text{crit},i} \tag{16}$$

Alternately, if we think of the fiber length as being variable while all other parameters are held constant, then the longest fiber length that cannot be broken in the flow (the "unbreakable length") is

$$L_{\text{ub}} = \left[\frac{\pi^3 E_f d_f^4}{4\zeta \eta_m \dot{\gamma}}\right]^{1/4} \tag{17}$$

and B_i is determined by the ratio of the actual fiber length to this unbreakable length,

$$B_i = (\ell_i/L_{\text{ub}})^4 \tag{18}$$

To translate these ideas about fiber buckling into a breakage probability, we first assume that P_i is proportional to the shear rate $\dot{\gamma}$, and to f_i, which is the fraction of fibers of length ℓ_i that have an orientation $\mathbf{p}$ such that $F_i(\mathbf{p})/F_{\text{crit}} \geqslant 1$.

$$P_i = (\text{const.})\dot{\gamma} f_i \tag{19}$$

We adopt the proportionality to shear rate based on the following: Consider two experiments at different shear rates, with the viscosities adjusted so that the shear stress is the same in both experiments. This gives the both experiments the same value of B_i, and we would expect to see the same amount of breakage in the two experiments if they have the same value of total shear strain. The proportionality of P_i to $\dot{\gamma}$ ensures that the model will behave in this way.

The function f_i depends on the probability distribution function for fiber orientation, $\psi(\mathbf{p})$. To guide model development, we calculated fiber orientation distributions using a discrete version of the Folgar–Tucker orientation model [36]. Details of the orientation calculation are give in Appendix B. Several different values of the rotary diffusion parameter were used, and the results are shown here in terms of the steady-state alignment in the flow direction, A_{11}. We focus the analysis on steady-state distributions in simple shear flow. This is reasonable, since most mold-filling flows are very nearly simple shear flow, and the orientation near the mold

walls, where stresses are highest and the most fiber breakage will occur, is typically close to the steady-state orientation for simple shear.

For each steady-state orientation distribution, and for each given value of B_i, we examine each fiber in our discrete orientation distribution function. Using Eq. (12), we evaluate the ratio of the compressive force on the fiber to the critical force for buckling force. The fraction of fibers for which this ratio is greater than or equal to unity is the value of f_i. This calculation is repeated over a range of B_i values.

The results, shown in Fig. 3, indicate that f_i equals zero for B_i equal to unity, and that f_i increases as B_i increases. f_i saturates at large values of B_i, with saturation values in the range of 0.10–0.05, depending on the degree of fiber alignment at steady state. This is consistent with our qualitative understanding from Fig. 2: even for very large values of B_i, only a fraction of the fibers will have an orientation in which the fiber is in compression. This fraction will decrease as the degree of fiber alignment increases, and fewer fibers are found in the regions of orientation space where they are loaded in compression.

Fig. 4 replots this same data, scaling each curve by its saturation value $f_{\max}$ and altering the horizontal axis to scaled fiber length using Eq. (18). The data falls more closely together now, suggesting that it would be reasonable to choose a single function $f_i/f_{\max}$ versus B_i for different fiber volume fractions and aspect ratios (which generate different steady-state values of A_{11}). Note that $f_{\max}$ depends on the fiber volume fraction and aspect ratio. In what follows we use a simple exponential function,

$$f_i = f_{\max}[1 - \exp(1 - B_i)] \tag{20}$$

This function is shown in Fig. 4 as the solid line. Clearly this function reproduces only the general trend of the calculated f_i values. While a better fit of the calculated f_i values could certainly be found, we have used Eq. (20) for two reasons. First, at this early stage of model development there is great uncertainty regarding many aspects of fiber breakage phenomena, so it makes sense not to over-refine the details of the model. And second, numerical experimentation [26] shows that the overall model results are not sensitive to the details of this function.

Substituting Eq. (20) into Eq. (19), we combine $f_{\max}$ with the remaining constant of proportionality, calling the product of these two factors C_B, the breakage coefficient. Our final model for the breakage probability P_i for fibers of length ℓ_i is then

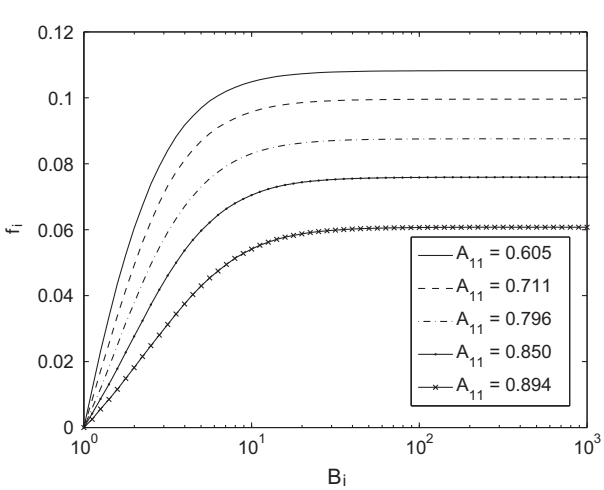

Fig. 3. Fraction f_i of fibers that have an orientation in which they can buckle, as a function of the buckling parameter B_i, for various steady-state orientations in simple shear flow.

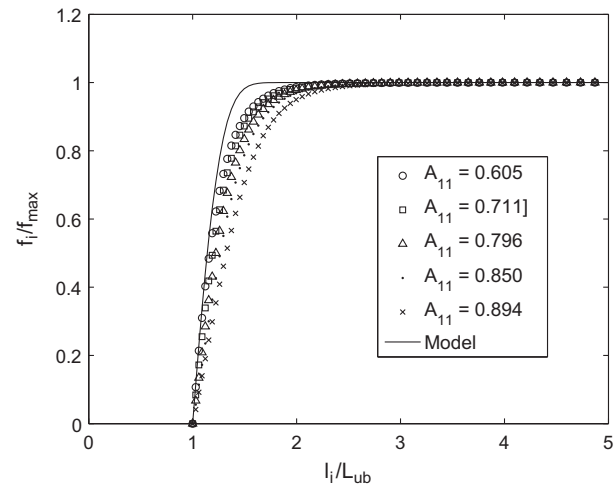

Fig. 4. Fraction f_i of fibers that have an orientation in which they can buckle, scaled by the maximum fraction at that orientation state $f_{\max}$, as a function of scaled fiber length. The line labeled "Model" is Eq. (20).

$$P_i = \begin{cases} 0 & \text{for} \quad B_i < 1 \\ C_B\dot{\gamma}[1 - \exp(1 - B_i)] & \text{for} \quad B_i \geqslant 1 \end{cases} \tag{21}$$

2.4. Child generation rates

Some assumptions must be made in order to develop a functional form for the child generation rates R_{ik}. First, the center of the fiber is the most likely location for breakage. Thus, the function R_{ik} should be maximum at $\ell_i = \ell_k/2$. Second, due to the effects of fiber–fiber interactions and material inconsistencies within the fiber, other locations along the fiber should have non-zero probabilities for breakage. From these requirements, it is reasonable to assume a Gaussian breakage profile, or

$$R_{ik} = \alpha_k N_{\text{PDF}}\left(\ell_i,\ \frac{\ell_k}{2},\ S\ell_k\right) \tag{22}$$

where $N_{\text{PDF}}()$ is the normal probability density function for the variable ℓ_i with mean $\ell_k/2$ and standard deviation $S\ell_k$, and α_k is a scale factor. The scale factor α_k is chosen to normalize R_{ik} in order to satisfy Eq. (8). This scales the child generation rates to match the breakage rates, and ensures conservation of total fiber length.

The variable S is a dimensionless fitting parameter that controls the shape of the Gaussian breakage profile. A small value of S corresponds to a high probability of breakage occurring near the fiber center, while a large S value distributes the probable breakage points more evenly along the fiber length. This completes the development of our model for flow-induced changes in the fiber length distribution.

2.5. Influence of model parameters

Our model has three parameters: C_B, ζ, and S. The breakage coefficient C_B controls the overall rate of change of fiber length, however the shapes that the fiber length distribution takes over time are independent of C_B, at least at constant shear rate. ζ is a hydrodynamic drag coefficient. It influences the force on the fiber through the expression for B_i, and thus it affects the length below which fibers do not break. S affects the shape of the fiber length distribution by affecting the distribution of child fibers produced when fibers break.

The influence of these parameters is illustrated in Figs. 5 and 6. Four different cases are shown here, and we use normalized

weight-based length distributions to facilitate comparison. All fiber lengths are normalized by L_{max}, the maximum initial length. The C_B parameter is accounted for by reporting results in terms of a dimensionless time, $t^* \equiv C_B\dot{\gamma}t$. S values of 0.2 and 1.0 bound the most useful values for this parameter. The value of ζ is combined with the flow stress and fiber properties to create a value for the unbreakable length (see Eq. (17)). $L_{ub}/L_{max} = 0.1$ represents a severe degradation of the initial fiber length, while $L_{ub}/L_{max} = 0.5$ is a very modest degradation of fiber length. The initial condition for all cases has a uniform weight distribution in the range $0.9L_{max}$ to L_{max}.

Fig. 5 shows data at $t^* = 2$, an intermediate time at which the fiber length distributions are changing rapidly. A portion of the initial distribution is apparent on the right side of the figure for all four cases. This demonstrates that our model can readily capture bimodal fiber length distributions. The influence of L_{ub} is clear, with peaks in the distributions developing around L_{ub} for all cases. The larger value of S tends to produce sharper peaks and a linear rise in the early part of the distribution, while the smaller value produces more rounded peaks. In our model fibers cannot break if $\ell_i < L_{ub}$, so the fibers in that range are all child fibers accumulated from the breakage of fibers with $\ell_i > L_{ub}$.

In Fig. 6 we see the fiber length distributions nearly at steady state, $t^* = 10$. The initial condition has disappeared, and most of the fibers now have lengths below L_{ub}. The length distributions look much more like experimental length distributions, and the effect of S is mainly visible for the case of $L_{ub}/L_{max} = 0.5$. For this case most of the fibers have experienced only one breakage event. For the other cases the fibers tend to have experienced a series of breakage events, which leads to the smoother-shaped length distributions.

As these examples show, ζ controls the location of the peak in the near-steady-state fiber length distribution, while C_B controls the time required to reach that state. S influences the exact shape of the fiber length distribution.

2.6. Relationship to model of Durin et al.

A fiber-length model very similar to the one presented here was recently reported by Durin et al. [24]. The two models are very similar, and indeed they share a common framework [26,37]. Both models calculate the time evolution of the full fiber length distribution, and both models assume that the mechanism of fiber breakage is buckling under hydrodynamic forces that load the fiber in compression. A quantitative comparison of the two models is beyond the scope of this paper, but we can outline the similarities and differences between the models here.

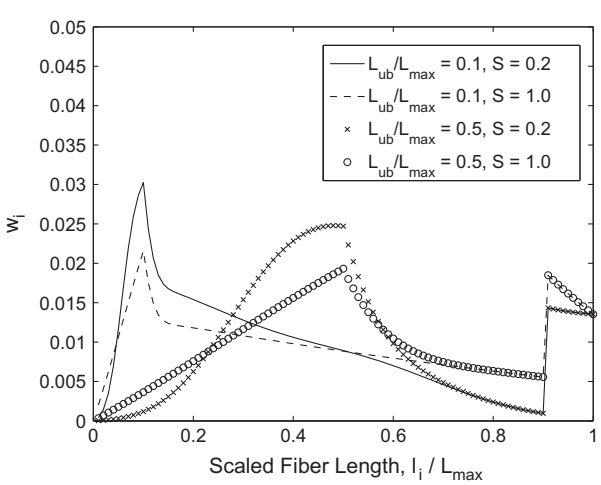

Fig. 5. Weight-based fiber length distributions at intermediate time, $t^* = 2$, for different values of the model parameters S and L_{ub} in steady simple shear flow. ($t^* \equiv C_B\dot{\gamma}t$).

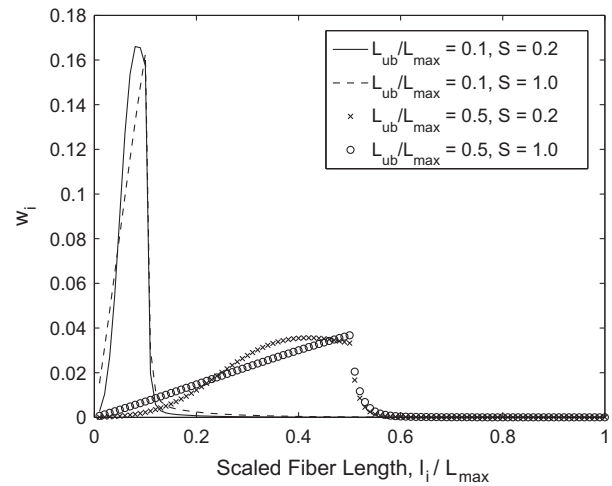

Fig. 6. Weight-based fiber length distributions at long time, $t^* = 10$, for different values of the model parameters S and L_{ub} in steady simple shear flow. ($t^* \equiv C_B\dot{\gamma}t$).

- The model of Durin et al. starts with a conservation equation that is equivalent to Eq. (9). Their main equation is posed in terms of the weight-based fiber length distribution (w_i in our notation) rather than the number-based distribution N_i, but conversion between the two forms is straightforward using Eq. (3). Thus, any differences between the two models must reside in the expressions for the breakage rate P_i and the child generation rate R_{ij}.
- Durin et al. build R_{ij} using a Weibull distribution of breakage probability along the fiber, while here we use a Gaussian distribution. They recommend using rather large values of the Weibull parameter, and in that range the Weibull distribution and the Gaussian distribution have very similar shapes. Their recommended range of the Weibull parameter is $m \geqslant 3$, which corresponds closely to $S \leqslant 0.8$ for our Gaussian distributions. Thus, the two models are actually quite similar in this aspect. Both the Weibull and Gaussian distributions are somewhat arbitrary choices; their use is justified by the fact that they produce fiber length distributions very similar to the ones observed experimentally.
- The same analysis of hydrodynamic forces on the fibers and fiber buckling is used in both papers. Durin et al. use a drag coefficient ζ based the Burgers [38] slender-body theory for a dilute suspension, while we maintain ζ as a model parameter. Our choice seems more appropriate for a highly concentrated suspension, but it does introduce an additional fitting parameter to the model. In both models, the elastic modulus E_f is the only mechanical property of the fiber that appears, and one might ask why the fiber strength is not present. Durin et al. [24] perform a detailed analysis of the stresses on a fiber with an initial curvature, which could potentially break before reaching the buckling load. They show that for properties typical of glass fibers this does not happen. Thus, fibers fracture by buckling, and the tensile strength of the fiber does not affect fiber breakage.
- The overall rate of fiber breakage in the Durin model is governed by the Jeffery orbit period of a fiber in a dilute suspension. This provides a physical motivation for making the breakage rate P_i proportional to $\dot{\gamma}$, just as it is in our model. The Jeffery period "for an average fiber" also provides the overall breakage

rate (roughly equivalent to C_B in our model), though their method of choosing the average fiber aspect ratio is not explained in detail.

- In our model a fiber whose breakage parameter is less than unity ($B_i < 1$, or $\ell_i < L_{ub}$) cannot break. In contrast, Durin et al. assign a non-zero, probability of breakage to fibers with $B_i < 1$. No explicit expression for P_i is given in their paper, but they certainly have $P_i > 0$ for some values of $B_i < 1$. This has little effect on the short-time behavior, and both models should produce rather similar results in the initial period of rapid degradation of fiber length. After this rapid initial decrease, fiber length will decrease more slowly in both models, but more rapidly in the model of Durin et al. than in our model.

Overall the two models are very similar, and they provide a sound framework upon which future efforts can build.

2.7. Implementation in a mold filling simulation

To implement our model in a mold filling simulation, one must calculate the fiber length distribution (a full set of N_i values) at each node in the mesh. We expect that fiber length will degrade more rapidly near the cavity walls, where the stresses are high, than near the midplane of the cavity, so fiber length data must be calculated at each node or layer across the thickness of the mold, as well as at each in-plane location.

A typical mold-filling simulation solves governing equations on a fixed mesh or grid. Thus, in Eq. (9) the time derivative d/dt must be replaced by the material derivative, and on a fixed grid we solve

$$\frac{\partial N_i}{\partial t} + \mathbf{v} \cdot \nabla N_i = -P_i N_i + \sum_k R_{ik} N_k \tag{23}$$

At each time step the results of the flow simulation provide the local shear rate, and viscosity. These are used to calculate the breakage rates and child generation rates. The fiber length distribution is typically updated using explicit time integration. This may be done on a smaller time step than the filling step in the molding simulation.

We have implemented our fiber length model in conjunction with the ORIENT mold filling code [16]. This code uses the Hele-Shaw formulation [39] and solves for filling, heat transfer, and fiber orientation in two simple mold geometries: an end-gated strip and a center-gated disk (Fig. 7). We use the suspension viscosity, determined from experimental measurements, in place of the matrix viscosity η_m when calculating breakage rates. At this stage of development we ignore any changes in suspension viscosity due to changes in fiber length. Thus, the fiber length calculations do not affect the filling or fiber orientation calculations. Also, the fiber orientation results do not affect the calculation of fiber lengths. This allows the fiber length calculation to be implemented as a post-processor to ORIENT. In this study we use a crude fountain-flow model, in which fiber-length data from the midplane node at the flow front is copied into nodal locations near the wall whenever a new column of nodes is filled by the advancing front. This algorithm probably overestimates the effect of the fountain flow. Additional details of the mold filling and fiber length calculations are given by Phelps [26].

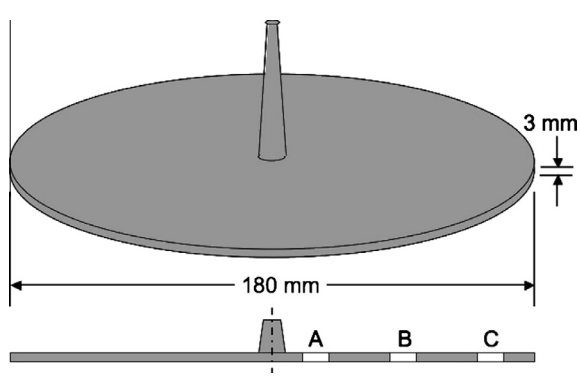

Fig. 7. Geometry and dimensions of center-gated disk moldings prepared by Pacific Northwest National Laboratory.

3. Experimental

3.1. Molding geometries, materials, and conditions

LFT samples were injection molded by Dr. James Holbery of the Pacific Northwest National Laboratory. The moldings feature matrices of polypropylene with reinforcement of 40% by weight glass fiber (MTI PP40G). These materials were compounded specifically for this study by Montsinger Technologies. The geometries were a 90 mm long × 80 mm wide end-gated ISO plaque [40] and a 180 mm diameter center-gated disk.

We focus here on sample AF3D, which is a center-gated disk molding with a fast filling speed. The geometry is shown in Fig. 7, the filling time was 0.65 s, the melt temperature was 510 K, and the mold wall temperature was 344 K. Material properties necessary for mold-filling simulations were either measured by Moldflow Plastics Labs, Kilsyth, Australia, or taken from the Moldflow Plastics Insight material library. Details are reported by Phelps [26]. Glass fiber properties for the breakage model are fiber modulus $E_f = 73$ GPa and fiber diameter $d_f = 17$ μm.

3.2. Measurement of fiber length

The usual approach for measuring the fiber length distribution is to burn off the polymer matrix, separate the fibers, and measure the fibers under a microscope, usually with the aid of image analysis software. While this approach is standard, the means of selecting the sample of fibers from the molding has not been standardized. It is likely that common methods, such as using tweezers to extract a group of fibers from the fiber mat that remains after burn-off, may preferentially sample the longer fibers or fibers from some portion of the thickness of the part, and thus produce a biased measurement.

To obtain an unbiased sample of fibers, we used a two-step sampling technique [41]. In the first step, the polymer matrix is burned away while the sample is constrained to its original sample size is a perforated metal container. This constraint prevents the fiber network from expanding, which it would otherwise do because of stored elastic energy in bent fibers. A hypodermic needle is then inserted into the constrained network, and a thin column of epoxy resin is injected. The epoxy is allowed to solidify, after which the surrounding fibers not encased in the epoxy column are gently removed. This isolates a region that samples uniformly the entire thickness of the molding. The epoxy column is then burned away so that the fibers can be separated, and the sample fibers are analyzed as in the standard technique. Even this method can preferentially select long fibers, since the diameter of the epoxy column is smaller than the length of the longest fibers. To account for this, a correction function is used in order to provide an unbiased fiber length distribution [41].

For each sample, fiber length measurements are made at locations A, B, and C, as shown in Fig. 7. These positions are centered approximately 15 mm, 45 mm, and 75 mm from the gate, respectively. Each region is three millimeters thick (the full thickness as the sample) and approximately 10 mm wide. At least 2300 individ-

ual fibers were measured at each location. The resulting data are averages of the fiber length distribution across the thickness of the molding. Our model predicts the fiber length distribution at multiple nodes across the cavity thickness, but in the comparisons that follow we average the predictions across the cavity thickness.

4. Results and discussion

The calculations use $\Delta\ell = 0.1$ mm and $n = 130$ length values to represent the fiber length distribution. This is a very detailed representation, which come at the cost of longer computing times. We use it here to ensure that the results are not distorted by a coarse discretization of the length distribution.

The length distribution Eq. (23) needs an inlet boundary condition for N_i. Here we use the experimental length data at location A ($x = 1.5$ cm from the gate) as the inlet condition at all points across the cavity thickness, and predict the results downstream of that. This is done because the ORIENT code cannot model flow in the gate region. A more sophisticated filling code could start the fiber length calculation further upstream, perhaps at the beginning of the runner system, using some information about the length distribution exiting the screw and nozzle.

All of the following results use $\zeta = 0.55$, $C_B = 0.025$, and $S = 1.0$. These values were determined empirically by adjusting them to produce a reasonable fit to the experimental data. The values themselves are physically reasonable in that we expect $\zeta \sim 1$ and $C_B \ll 1$. Also, $S = 1.0$ distributes the breakage location along each fiber, while retaining a preference for breaking fibers near their centers.

Fig. 8 shows a portion of the fiber length data calculated by our model for this molding. In this figure, the length distribution at each node has been used to calculate nodal weight-average lengths L_w according to Eq. (5). The resulting values are used to draw the contours in the figure. We see that the fibers remain long (red colors in the figure) near the midplane ($z = 0$), due to the low shear stress and low accumulation of shear strain there. Closer to the mold wall we see shorter fiber lengths (blue colors), owing to the higher shear stresses and greater accumulated shear strain. The region with shorter fibers becomes thicker with increasing distance from the gate. Very close to the cavity wall the fibers remain fairly long; this is material that traveled along the midplane, caught up to the flow front, and was then pushed to the mold walls by the fountain flow. It froze there quickly, so that it experienced very little shear strain at the high stress levels near the wall. The thickness of this region is also greater the farther away one is from the gate.

Figs. 9 and 10 compare the measured fiber length distributions at positions B and C with the predictions of the model. The predicted length distributions are very similar in character to the measured distributions. Note that both the experimental and predicted distributions are averaged across the cavity thickness.

As Figs. 1, 9 and 10 show, our samples have very few fibers that are longer than 6 mm, and the average fiber lengths range from 1.5 to 3.0 mm. This indicates that the fiber length is highly degraded in this particular molding. In other injection-molding experiments, to be reported at a later date, we have seen significant numbers of longer fibers. The fiber length distributions in these samples are bimodal, a feature that is readily reproduced in our model, as demonstrated in Fig. 5.

A quantitative comparison between the experiment and our predictions appears in Fig. 11, which shows the average lengths

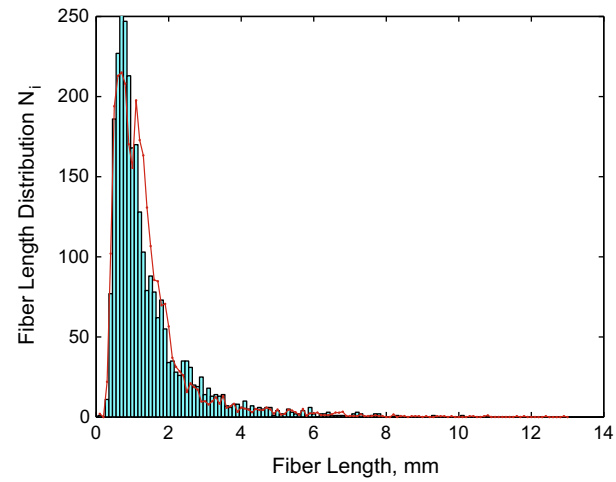

Fig. 9. Experimental (bars) and predicted (line with dots) fiber length distribution at position B for sample AF3D. (For interpretation of the references to color in this figure legend, the reader is referred to the web version of this article.)

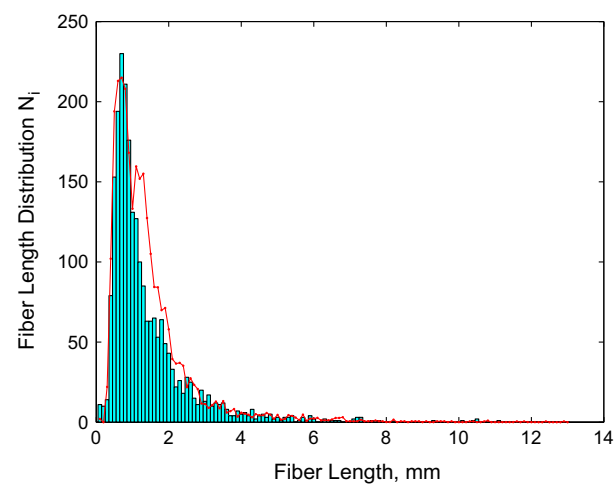

Fig. 10. Experimental (bars) and predicted (line with dots) fiber length distribution at position C for sample AF3D. (For interpretation of the references to color in this figure legend, the reader is referred to the web version of this article.)

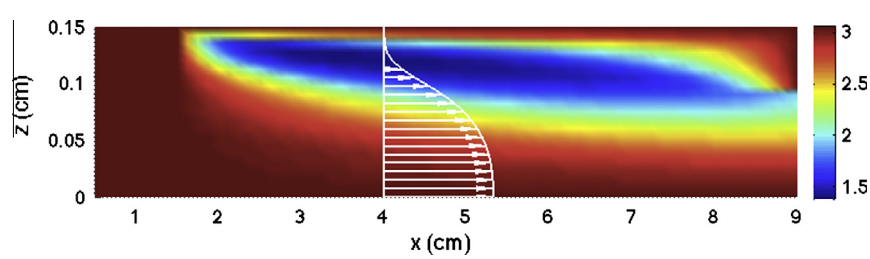

Fig. 8. Contours of weight-average fiber length L_w versus position in the mold cavity, predicted for sample AF3D. Colorbar gives L_w in mm. x measures distance along the flow path, starting just downstream of the gate. z measures distance from the cavity midplane. The arrows indicate the velocity profile at $x = 4$ cm.

as a function of distance along the flow path. The predicted curves are flat for $x < 1.5$ cm, because the fiber length calculations actually start at this location, which is point A. Average fiber length (again, averaged across the part thickness) initially decreases with flow length. This is because fibers farther down the flow path have experienced greater shear strains, and thus have had more opportunity to break. The weight-average length decreases more rapidly than the number-average length, because it is more sensitive to the number of very long fibers, and these fibers are the most likely to break. Closer to the end of the flow path both of the average lengths increase. This is a result of the fountain effect, as discussed in connection with Fig. 8. The model is quite a good fit for this experimental data, though the changes in average fiber length are fairly modest in this particular example.

5. Conclusions

In long-fiber thermoplastic composites, changes in the fiber length distribution due to processing can be significant, and can affect the mechanical properties of the final material. We have developed a quantitative model than can predict these changes. Local microstructure is represented by a discrete version of the fiber length distribution. A balance equation for the length distribution is written. A model for the breakage rate is then developed, using the concept that fibers break by buckling under hydrodynamically-induced compressive forces in certain unfavorable orientations relative to the flow. The resulting model can be implemented in a conventional injection mold filling simulation. Preliminary results show very good agreement with experiments on a glass fiber/polypropylene LFT, molded in a center-gated disk geometry.

In the experiments presented here, the effect of changes in fiber length on the stiffness of the molded part is quite modest. Using the micromechanics calculations described in Nguyen et al. [25], the difference in elastic modulus between the maximum fiber length of 13 mm and the observed average fiber length of approximately 1.5 mm is only about 5%. This difference is small because even at 1.5 mm average fiber length the average fiber aspect ratio is approximately 90, and elastic modulus is not sensitive to fiber aspect ratio in this range. However, tensile strength does continue to improve with fiber length in this range, and toughness improves even more [11]. This highlights the value of a model that calculates the entire fiber length distribution, and can capture any very long fibers that survive the processing.

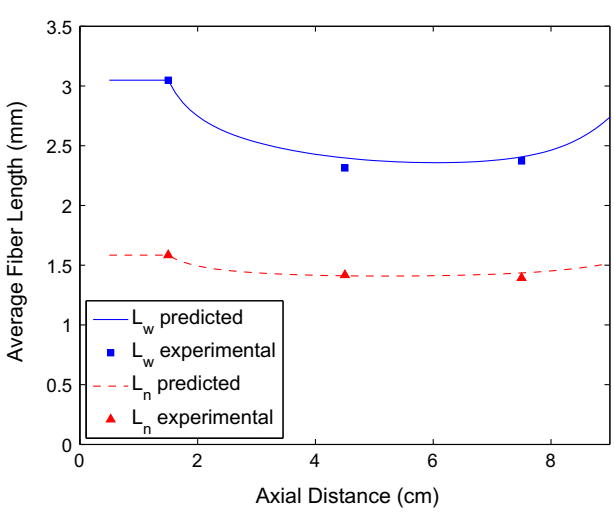

Fig. 11. Experimental and predicted average fiber lengths as a function of flow distance for sample AF3D. Predictions begin at point A ($x = 1.5$ cm), using the measured length distribution there as the initial condition. (For interpretation of the references to color in this figure legend, the reader is referred to the web version of this article.)

Our present model is very promising. Many refinements of the model are possible within the framework that we have developed here. The basic conservation equation will not change, but one could introduce more detailed modeling and perhaps additional physics into the breakage rate model for P_i. Breakage rate could include a dependence on the fiber orientation state relative to the flow, or it could incorporate the loading from fiber–fiber contacts. Some careful, basic experiments to measure directly the breakage rates in a well-defined flow would be highly desirable, and such empirical knowledge could be incorporated into the theoretical framework developed here.

The model we have developed also provides some insights into the way that simpler models like those of Shon et al. [23], Inceoglu et al. [21] might be improved. In our model, the overall rate of reduction of fiber length scales with $C_B\dot{\gamma}$. Replacing the terms k_f or K''SME in Eqs. (1) and (2) with an expression like $C_B\dot{\gamma}$ would provide the desired scaling with shear rate. The effect of flow stress could then be introduced by making the equilibrium lengths L_∞ or $L_{w\infty}$ depend on stress in a manner similar to L_{ub} in Eq. (17). Of course these models only predict an average fiber length, whereas our model and the model of Durin et al. [24] predict the entire fiber length distribution.

Our model as it stands can be implemented with almost any flow solver, whether for injection molding (Hele-Shaw or true 3-D), or in software for other processes such as extrusion compounding. The large number of variables at each node used to represent the length distribution does make the computations expensive, particularly for large parts. One approach to resolving this issue is to use a coarser discretization of the length distribution, leading to fewer N_i values at each nodel. Another possibility is to develop an approach similar to that used for fiber orientation, where a few parameters are used to characterize the distribution function, and equations are derived for those parameters starting from the governing equations of the distribution function [15]. This remains as a potential task for future research.

Acknowledgements

This research was sponsored by the US Department of Energy, Office of Energy Efficiency and Renewable Energy, Vehicle Technologies Program, as part of the Lightweight Materials Program under contract DE-AC05-00OR22725 with UT-Battelle, LLC. Comments and suggestions from Drs. Mark T. Smith, Ba Nghiep Nguyen, and James D. Holbery of Pacific Northwest National Laboratory, and from the industrial advisory board of the project, are gratefully acknowledged. We also thank Drs. Xiaoshi Jin and Jin Wang of Autodesk Moldflow for their helpful insights and suggestions.

Appendix A

To derive Eq. (10) for the hydrodynamic force acting to compress a fiber, consider a fiber with a unit orientation vector $\mathbf{p}$ and a local coordinate s along the fiber length. Let $s = 0$ at the centroid of the fiber, so s ranges from $\ell_i/2$ to $-\ell_i/2$. Following Dinh and Armstrong [30], the increment of force $d\mathbf{f}$ on an increment of fiber length ds due to hydrodynamic loading is

$$d\mathbf{f} = \zeta_{\text{eff}} \cdot (\mathbf{v} - \dot{\mathbf{r}})ds \tag{24}$$

where ζ_{eff} is a tensorial anisotropic drag coefficient, $\mathbf{v}$ is the unperturbed fluid velocity at the given point along the fiber axis, and $\dot{\mathbf{r}}$ is the rate of change of the position vector $\mathbf{r}$, which extends from the origin to the given material point on the fiber.

Defining $\mathbf{r}_c$ to be the position vector of the centroid of the fiber, we can write $\mathbf{r}$ as:

$$\mathbf{r} = \mathbf{r}_c + s\mathbf{p} \tag{25}$$

Allowing $\mathbf{v}_o$ to represent the velocity of the (arbitrarily selected) origin, the unperturbed fluid velocity $\mathbf{v}$ at any point along the fiber is then

$$\mathbf{v} = \mathbf{v}_o + \mathbf{L}\cdot\mathbf{r} \tag{26}$$

where $\mathbf{L}$ is the velocity gradient tensor ($L_{ij} = \partial\, v_i/\partial x_j$), and we have assumed that $\mathbf{v}$ is approximately linear in $\mathbf{r}$ over the fiber length.

If only hydrodynamic forces act then the centroid of the fiber moves with the unperturbed fluid velocity of $\mathbf{r}_c$ [30], so the rate of change of $\mathbf{r}_c$ is

$$\dot{\mathbf{r}}_c = \mathbf{v}_o + \mathbf{L}\cdot\mathbf{r}_c \tag{27}$$

Combining Eqs. (25)–(27) and simplifying gives

$$\mathbf{v} - \dot{\mathbf{r}} = s(\mathbf{L}\cdot\mathbf{p} - \dot{\mathbf{p}}) \tag{28}$$

Note that $\dot{\mathbf{p}}$ describes the rate of rotation of the fiber axis. For this we use Jeffery's equation,

$$\dot{\mathbf{p}} = \mathbf{W}\cdot\mathbf{p} + \xi(\mathbf{D}\cdot\mathbf{p} - \mathbf{D}:\mathbf{ppp}) \tag{29}$$

where $\mathbf{W} = \frac{1}{2}(\mathbf{L} - \mathbf{L}^T)$ is the vorticity tensor and $\mathbf{D} = \frac{1}{2}(\mathbf{L} + \mathbf{L}^T)$ is the rate-of-deformation tensor. The scalar ξ is the shape parameter, which approaches unity for slender fibers. In the limit of $\xi \to 1$, Eq. (29) may be recast in terms of $\mathbf{L}$, to give

$$\dot{\mathbf{p}} = \mathbf{L}\cdot\mathbf{p} - \mathbf{L}:\ \mathbf{ppp} \tag{30}$$

Note that $\mathbf{W}$: $\mathbf{pp}$ = 0, owing to the anti-symmetry of $\mathbf{W}$.

Combining (30) with Eqs. (24) and (28) gives the increment of force on a slice ds of the fiber as

$$d\mathbf{f} = (\boldsymbol{\zeta}_{\text{eff}}\cdot\mathbf{p})(\mathbf{D}:\ \mathbf{pp})\ s\ ds \tag{31}$$

Dinh and Armstrong [30] note that the drag tensor $\boldsymbol{\zeta}_{\text{eff}}$ may be decomposed into a component transverse to the fiber axis and a component parallel to the fiber axis, or:

$$\boldsymbol{\zeta}_{\text{eff}} = \zeta_t(\mathbf{I} - \mathbf{pp}) + \zeta_p\mathbf{pp} \tag{32}$$

where ζ_t and ζ_p are scalar drag coefficients. Substituting this into Eq. (31) shows that only the parallel drag coefficient ζ_p matters for force on the fiber. Again following Dinh and Armstrong, both drag coefficients scale with the matrix viscosity η_m, so we write $\zeta_p = \zeta\eta_m$, where ζ (no subscript) is a dimensionless drag coefficient. Using this in (31) gives an explicit expression for the increment of force on a segment of a fiber,

$$d\mathbf{f} = \zeta\eta_m\mathbf{p}(\mathbf{D}:\ \mathbf{pp})\ s\ ds \tag{33}$$

The force $d\mathbf{f}$ acts parallel to the fiber axis; it is proportional to the fluid stretch rate parallel to that axis, ($\mathbf{D}$: $\mathbf{pp}$), and to the distance s from the centroid of the fiber.

Since the fiber center is the most likely location for buckling to occur, we integrate from $s = 0$ to $s = \ell_i/2$ to find the force vector $\mathbf{f}_c$ at the fiber centroid.

$$\mathbf{f}_c \equiv \int_{s=0}^{s=\ell_i/2} d\mathbf{f} \tag{34}$$

Substituting Eq. (33) and evaluating the integral, we find

$$\mathbf{f}_c = \frac{\zeta\eta_m\ell_i^2}{8}\ \mathbf{p}\ (\mathbf{D}:\ \mathbf{pp}) \tag{35}$$

For the analysis of fiber buckling we need a scalar value of force at the centroid F_i, defined such that F_i is positive when the fiber is in compression. Since $\mathbf{f}_c$ is directed along the $\mathbf{p}$ axis, this means that $F_i \equiv -\mathbf{f}_c\cdot\mathbf{p}$, and we have

$$F_i = \frac{\zeta\eta_m\ell_i^2}{8}\ (-\mathbf{D}:\ \mathbf{pp}) \tag{36}$$

which is Eq. (10).

Appendix B

To evaluate f_i in Eq. (19) we use a discrete approximation to the fiber orientation distribution, $\psi_i(\mathbf{p})$. This is formed using a large number of unit orientation vectors $\mathbf{p}_k$, with $k = 1$ to n_p. Typically, n_p = 10,000. These vectors are initialized in some convenient way, in this case random in 3-D space, and are then subject to a time history that corresponds to their motion in simple shear flow. After a sufficient amount of time the family of vectors reach a statistical steady state, and they form a representative sample of the orientation distribution $\psi_i(\mathbf{p})$.

Here we use the original model of Folgar and Tucker [36], which has an isotropic rotary diffusivity, and use the limit of high particle aspect ratio, $\xi \to 1$. In this limit the deterministic part of the fiber motion gives a new orientation for any finite time step Δt as

$$\mathbf{p}_k^* = \frac{\mathbf{F}\cdot\mathbf{p}_k}{|\mathbf{F}\cdot\mathbf{p}_k|} \tag{37}$$

where $\mathbf{F}$ is the deformation gradient tensor over the time step. For 1–3 simple shear flow, this is

$$\mathbf{F} = \begin{bmatrix} 1 & 0 & \dot{\gamma}\Delta t \\ 0 & 1 & 0 \\ 0 & 0 & 1 \end{bmatrix} \tag{38}$$

Our calculation uses a small time step ($\dot{\gamma}\Delta t = 0.05$), and introduces the rotary diffusion term stochastically by adding a small random perturbation $\Delta\mathbf{p}_k$ to each orientation vector. Thus, in our calculation the new value of orientation at each time step is calculated from the previous value $\mathbf{p}_k$ by first calculating $\mathbf{p}_k^*$ using Eq. (37), and then adding a random component $\Delta\mathbf{p}_k$ according to

$$\mathbf{p}_k^{\text{new}} = \frac{\mathbf{p}_k^* + \Delta\mathbf{p}_k}{|\mathbf{p}_k^* + \Delta\mathbf{p}_k|} \tag{39}$$

The random perturbation $\Delta\mathbf{p}_k$ is chosen to be uniformly distributed on a small circular disk normal to the original vector. For each $\mathbf{p}_k$ we determine mutually orthogonal unit vectors $\mathbf{s}_k$ and $\mathbf{t}_k$, and then find the perturbation as

$$\Delta\mathbf{p}_k = r_k(\cos\phi_k\mathbf{s}_k + \sin\phi_k\mathbf{t}_k) \tag{40}$$

Here the angles ϕ_k are uniformly distributed on $[0, 2\pi)$ and the scalar magnitudes r_k are given by

$$r_k = Q\sqrt{q_k} \tag{41}$$

Q is a scale factor that is constant for the entire calculation, and each q_k is uniformly distributed on $[0, 1)$. With this calculation we expect that the rotary diffusivity $C_I\dot{\gamma}$ will scale approximately with $Q^2/\Delta t$.

Our calculations use 10,000 $\mathbf{p}$ vectors and $\dot{\gamma}\Delta t = 0.05$. The initial orientation state is random in 3-D, and the calculation is run for 1500 steps (75 strain units) to reach a steady state orientation. An additional 500 time steps are run, and the results of all 500 steps

Table 1
Correspondence between orientation perturbation parameter Q, steady-state orientation in the flow direction, and corresponding interaction coefficient C_I using the ORE closure, for the fiber orientation distribution calculations in Appendix B.

$Q^2/\dot{\gamma}\ \Delta t$	Q	$A_{11,\text{steady}}$	$C_{I,\text{ORE}}$
0.30	0.1225	0.6051	0.0443
0.10	0.0707	0.7111	0.0184
0.03	0.0387	0.7958	0.00776
0.01	0.0224	0.8504	0.00377
0.003	0.0122	0.8938	0.0176

are combined to get the steady-state orientation tensor. A series of B_i values are then considered, and the set of orientation vectors from the final time step are used to compute f_i, the fraction of fibers that could buckle and break, for each B_i according to Eq. (12).

The results are shown in Fig. 3, labeled according to the steady-state orientation in the flow direction, A_{11}. Table 1 shows the correspondence between the Q values used in each calculation and the steady-state values of A_{11}. Also shown here are the C_I values that give the same steady-state value of A_{11} when used in the moment-tensor equations for fiber orientation [15], with the ORE version of the orthotropic closure approximation [42,43]. Note that other closure approximations will require different values of C_I to get the same A_{11} value.

References

[1] Cattanach JB, Cuff G, Cogswell FN. The processing of thermoplastics containing high loadings of long and continuous reinforcing fibers. J Polym Eng 1986;6:345–62.
[2] Marshall DF. Long-fibre reinforced thermoplastics. Mater Des 1987;8:77–81.
[3] Creasy TS, Advani SG. Transient rheological behaviour of a long discontinuous fiber-melt system. J Rheol 1996;40:497–519.
[4] Cervenka A, Allan PS. Characterization of finite length composites: Part III. Studies on thin sections extracted from moldings (wafers). Pure Appl Chem 1997;69:1725–40.
[5] Glas L, Allan PS, Vu-Khanh T, Cervenka A. Characterization of finite length composites: Part II. Mechanical performance of injection molded composites. Pure Appl Chem 1997;69:1707–23.
[6] Bailey RS, Kraft H. A study of fibre attrition in the processing of long-fibre reinforced thermoplastics. Int Polym Process 1987;2:94–101.
[7] Denault J, Vu-Khanh T, Foster B. Tensile properties of injection molded long fiber thermoplastic composites. Polym Compos 1989;10:313–21.
[8] Spahr DE, Friedrich K, Schultz JM, Bailey RS. Microstructure and fracture behaviour of short and long fibre-reinforced polypropylene composites. J Mater Sci 1990;25:4427–39.
[9] Bush SF, Torres FG, Methven JM. Rheological characterisation of discrete long glass fibre (LGF) reinforced thermoplastics. Composites A 2000;31:1421–31.
[10] Gleissle W, Curry J. Characterization of finite length composites. Int Polym Process 2003;18:20–32.
[11] Thomason JL. The influence of fibre length and concentration on the properties of glass fibre reinforced polypropylene: 6. The properties of injection moulded long fibre PP at high fibre content. Composites A 2005;36:995–1003.
[12] Vu-Khanh T, Denault J, Habib P, Low A. The effects of injection molding on the mechanical behavior of long-fiber reinforced PBT/PET blends. Compos Sci Technol 1991;40:423–35.
[13] Skourlis TP, Pochiraju K, Chassapis C, Manoochehri S. Structure-modulus relationships for injection-molded long fiber-reinforced polyphthalamides. Composites B 1998;29:309–20.
[14] Stokes VK, Inzinna LP, Liang EW, Trantina GG, Woods JT. A phenomenological study of the mechanical properties of long-fibre filled injection-molded thermoplastic composites. Polym Compos 2000;21:696–710.
[15] Advani SG, Tucker III CL. The use of tensors to describe and predict fiber orientation in short fiber composites. J Rheol 1987;31:751–84.
[16] Bay RS, Tucker III CL. Fiber orientation in simple injection moldings. Part I: theory and numerical methods. Polym Compos 1992;13(4):317–31.
[17] Bay RS, Tucker III CL. Fiber orientation in simple injection moldings. Part II: experimental results. Polym Compos 1992;13(4):332–42.
[18] Phelps JH, Tucker III CL. An anisotropic rotary diffusion model for fiber orientation in short- and long-fiber thermoplastics. J Non-Newtonian Fluid Mech 2009;156:165–76.
[19] O'Regan D, Akay M. The distribution of fibre lengths in injection moulded polyamide composite components. J Mater Process Technol 1996;56:282–91.
[20] LaFranche E, Krawczak P, Ciolczyk JP, Maugey J. Injection moulding of long glass fiber reinforced polyamide 66: processing conditions/microstructure/flexural properties relationship. Adv Polym Technol 2005;24:114–31.
[21] Inceoglu F, Ville J, Ghamri N, Pradel JL, Durin A, Valette R, et al. Correlations between processing conditions and fiber breakage during compounding of glass fiber-reinforced polyamide. Polymer Compos 2011;32(11):1842–50.
[22] Shimizu Y, Arai S, Itoyama T, Kawamoto H. Experimental analysis of the kneading disk region in a co-rotating twin screw extruder: Part 2. Glass–fiber degradation during compounding. Adv Polym Technol 1997;16(1):25–32.
[23] Shon K, Liu D, White JL. Experimental studies and modeling of development of dispersion and fiber damage in continuous compounding. Int Polym Proc 2005;20(3):322–31.
[24] Durin A, De Micheli P, Ville J, Inceoglu F, Valette R, Vergnes B. A matricial approach of fibre breakage in twin-screw extrusion of glass fibres reinforced thermoplastics. Composites A 2013;48:47–56.
[25] Nguyen BN, Kunc V, Frame B, Phelps JH, Tucker III CL, Bapanapalli SK, et al. Prediction of the elastic-plastic stress/strain response for injection-molded long-fiber thermoplastics. J Compos Mater 2009;43:217–46.
[26] Phelps JH. Processing-microstructure models for short- and long-fiber thermoplastic composites. Ph.D. thesis. University of Illinois at Urbana-Champaign; 2009.
[27] Toll S. Packing mechanics of fiber reinforcements. Polym Eng Sci 1998;38(8):1337–50.
[28] Djalili-Moghaddam M, Toll S. A model for short-range interactions in fibre suspensions. J Non-Newtonian Fluid Mech 2005;132:73–83.
[29] von Turkovich R, Erwin L. Fiber fracture in reinforced thermoplastic processing. Polym Eng Sci 1983;23:743–9.
[30] Dinh SM, Armstrong RC. A rheological equation of state for semiconcentrated fiber suspensions. J Rheol 1984;28(3):207–27.
[31] Shaqfeh ESG, Fredrickson GH. The hydrodynamic stress in a suspension of rods. Phys Fluids A 1990;2(1):7–24.
[32] Jeffery GB. The motion of ellipsoidal particles immersed in a viscous fluid. Proc Roy Soc 1922;A102:161–79.
[33] Forgacs OL, Mason SG. Particle motions in sheared suspensions IX: spin and deformation of threadlike particles. J Colloid Sci 1959;14:457–72.
[34] Salinas A, Pittman JFT. Bending and breaking fibers in sheared suspensions. Polym Eng Sci 1981;21(1):23–31.
[35] Hernandez JP, Raush T, Rios A, Strauss S, Osswald TA. Theoretical analysis of fiber motion and loads during flow. Polym Compos 2004;25:1–11.
[36] Folgar F, Tucker III CL. Orientation behavior of fibers in concentrated suspensions. J Reinf Plast Compos 1984;3:98–119.
[37] Tucker CL, Phelps JH, Abd El-Rahman, AI, Kunc V, Frame BJ. Modeling fiber length attrition in molded long-fiber composites. In: Proceedings of the polymer processing society 26th annual meeting – PPS-26. Canada: Banff; 2010.
[38] Burgers JM. On the motion of small particles of elongated form, suspended in a viscous liquid. In: Second report on viscosity and plasticity. New York: Nordemann Publishing; 1938.
[39] Hieber CA, Shen SF. A finite-element/finite-difference simulation of the injection-molding filling process. J Non-Newtonian Fluid Mech 1980;7:1–32.
[40] International organization for standardization. Plastics – injection moulding of test specimens for thermoplastic materials – Part 5: preparation of standard specimens for investigation anisotropy; 2001. [ISO 294-5:2001].
[41] Kunc V, Frame BJ, Nguyen BN, Tucker III C, Velez-Garcia G. Fiber length distribution measurement for long glass and carbon fiber reinforced injection molded thermoplastics. In: Proceedings of the 7th annual society of plastic engineers automotive composites conference and exposition. MI: Troy; 2007.
[42] Cintra Jr JS, Tucker III CL. Orthotropic closure approximations for flow-induced fiber orientation. J Rheol 1995;39:1095–122.
[43] VerWeyst BE. Numerical predictions of flow-induced fiber orientation in 3-d geometries. Ph.D. thesis. Urbana (IL): University of Illinois at Urbana-Champaign; 1998.